

FAST ACCURATE APPROXIMATION OF CONVOLUTIONS WITH WEAKLY SINGULAR KERNEL AND ITS APPLICATIONS

AWANISH KUMAR TIWARI, AMBUJ PANDEY, JAGABANDHU PAUL, AND AKASH ANAND

ABSTRACT. In this article, we present an $O(N \log N)$ rapidly convergent algorithm for the numerical approximation of the convolution integral with radially symmetric weakly singular kernels and compactly supported densities. To achieve the reduced computational complexity, we utilize the Fast Fourier Transform (FFT) on a uniform grid of size N for approximating the convolution. To facilitate this and maintain the accuracy, we primarily rely on a periodic Fourier extension of the density with a suitably large period depending on the support of the density. The rate of convergence of the method increases with increasing smoothness of the periodic extension and, in fact, approximations exhibit super-algebraic convergence when the extension is infinitely differentiable. Furthermore, when the density has jump discontinuities, we utilize a certain Fourier smoothing technique to accelerate the convergence to achieve the quadratic rate in the overall approximation. Finally, we apply the integration scheme for numerical solution of certain partial differential equations. Moreover, we apply the quadrature to obtain a fast and high-order Nystöm solver for the solution of the Lippmann-Schwinger integral equation. We validate the performance of the proposed scheme in terms of accuracy as well as computational efficiency through a variety of numerical experiments.

1. INTRODUCTION

In this article, we propose an $O(N \log N)$ rapidly convergent algorithm for numerical approximation of the convolution operator of the form

$$(1) \quad (Au)(x) = \int_D g(x-y)u(y) dy$$

with a weakly singular kernel g and a smooth density u whose support is contained in D which, without loss of generality, we assume to be the unit square, that is, $D = [0, 1] \times [0, 1]$. The convolution integral of the form eq. (1) arise in a wide range of application areas, for instance, fluid dynamics [16], quantum physics [4], and electromagnetism [6], to name a few. In particular, utilizing the proposed numerical scheme, we construct fast solvers for two important problems. For the first set of problems, we obtain solutions to certain linear constant-coefficient partial differential equations that arise, for example, in electrostatics and fluid dynamics. For the second problem, we solve the Lippmann-Schwinger integral equation whose application areas include wave propagation and scattering [13], medical imaging [11, 12, 28], and Radar imaging [9].

In the literature, several fast, high-order algorithms are available, especially in the context of Helmholtz and Laplace kernels. In particular, most convolutions where $g(x)$ is the fundamental solution of the Laplace equation arise in the context of the Poisson problem [17]. For a concise review on the more general problem of numerical solution of constant-coefficient partial differential equations, we refer the readers to [3, 18, 19]. On the other

hand, most solvers involving the Helmholtz kernel are devoted to the numerical solution of the Lippmann-Schwinger integral equation [13, page 216]. While we do not intend to review all such work here, some recent contributions in this direction can be found in [1, 2, 5, 6, 10, 14, 15, 17, 21, 22, 24, 25] and references therein. To the best of our knowledge, none of the methods cited above are designed to handle the more general class of weakly singular kernels. A notable exception is the method proposed in [29] that can handle a large class of weakly singular kernels. The key idea in [29] is to truncate the underlying kernel so that the value of convolution integral eq. (1) remains unchanged. As a result, by the Paley-Wiener theorem, the Fourier transform of the whole integrand is infinitely smooth, and subsequently, an accurate approximation of eq. (1) is obtained by evaluating the inverse Fourier transform of smooth functions. While the method is easy to implement and converges fast, its applicability is constrained by the availability of an analytical expression of the Fourier transform of the underlying truncated singular kernels, which, in general, is not available.

The proposed numerical scheme achieves the desired $O(N \log N)$ computational complexity by employing the Fast Fourier Transform (FFT) based on equispaced Cartesian grids and is applicable to any weakly singular kernel. The method converges super-algebraically provided the density u is infinitely differentiable in D and all its derivatives vanish at the boundary of D . As we see in the next section, the proposed integration scheme requires computation of certain moments. For some special kernels, including those coming from the fundamental solution of the Laplace and the Helmholtz equation, analytic expressions are available for these moments. In such cases, our method reduces to a straightforward application of the two-dimensional FFT. However, more generally, when such exact expressions are not available, we can obtain them numerically to a desired level of accuracy. For example, we discuss one such approach to pre-compute their high-order numerical approximations. Even though this pre-computation is needed to be performed only once for each weakly singular kernel, the accompanying cost can be reduced dramatically by invoking a specific localization technique. Moreover, in the case when u is only piecewise smooth, we utilize a certain Fourier smoothing technique [6, 27] to enhance the linear rate of convergence to achieve approximations that converge quadratically.

The organization of the paper is as follows. We present the proposed numerical integration scheme to approximate the convolution integral (1) in Section 2. We begin, in Section 2.1, with an introduction to the numerical method and follow it up, in Section 2.2, with a discussion on the computation of certain moments that are needed in the method. In Section 2.3, we discuss the localized integration scheme to reduce the pre-computation cost when an analytic expression for obtaining these moments is not available. Next, to improve the convergence rate for piecewise smooth densities, a Fourier smoothed integration scheme is discussed in Section 2.4. Finally, we present a variety of numerical results to validate the performance and applicability of the proposed method in Section 3. In particular, in Section 3.1, we conduct extensive numerical experiments to computationally establish the expected convergence rates of our scheme. Moreover, we also include a test to confirm the $O(N \log N)$ computational complexity of the method. Further, in Section 3.2 and Section 3.3, we apply the integration scheme to solve Poisson and Lippmann-Schwinger equation, respectively, in a variety of settings. Some concluding remarks along with some future directions are put forth in Section 4.

2. THE NUMERICAL INTEGRATION SCHEME

This section presents a detailed description of our numerical scheme for the approximation of eq. (1).

2.1. Basic Idea. Toward obtaining an approximation to eq. (1), we begin by considering the b -periodic extension u_e of u by

$$(2) \quad u_e(x) = \begin{cases} u(x), & x \in D \\ 0, & x \in D_e \setminus D, \end{cases}$$

where $D_e = [0, b]^2$, and b is an integer with $b \geq 1 + \sqrt{2}$. If $B_a(x)$ denotes the ball of radius a centered at x , then for all a satisfying $\sqrt{2} \leq a \leq b - 1$ and all $x \in D$, we have $D \subseteq B_a(x) \subseteq [-(b - 1), b]^2$, so that

$$(3) \quad (Au)(x) = \int_D g(x - y)u(y)dy = \int_D g(x - y)u_e(y)dy = \int_{B_a(x)} g(x - y)u_e(y)dy.$$

Using the b -periodicity of u_e , the last integral in eq. (3) is expressed as

$$(4) \quad (Au)(x) = \sum_{k \in \mathbb{Z}^2} \widehat{g}(k) \widehat{u}_e(k) e^{2\pi i k \cdot x/b},$$

where

$$(5) \quad \widehat{g}(k) = \int_{B_a(0)} g(y) e^{-2\pi i k \cdot y/b} dy, \quad \widehat{u}_e(k) = \frac{1}{b^2} \int_{D_e} u_e(y) e^{-2\pi i k \cdot y/b} dy.$$

In view of eq. (4) and eq. (5), we take the numerical integration scheme A_n to be of the form

$$(6) \quad (A_n u)(x) = \sum_{k \in \mathbb{F}_n} \widehat{g}(k) \widehat{u}_{e,n}(k) e^{2\pi i k \cdot x/b},$$

where

$$\mathbb{F}_n = \begin{cases} \mathbb{Z}^2 \cap [-nb/2, nb/2]^2, & nb \text{ is even,} \\ \mathbb{Z}^2 \cap [-(nb - 1)/2, (nb - 1)/2]^2, & nb \text{ is odd,} \end{cases}$$

and $\widehat{u}_{e,n}(k)$ is the trapezoidal approximation of $\widehat{u}_e(k)$ given by

$$\widehat{u}_{e,n}(k) = \frac{1}{(nb)^2} \sum_{j \in \mathbb{G}_n} u_j e^{-2\pi i k \cdot j/nb},$$

where $\mathbb{G}_n = \mathbb{Z}^2 \cap ([0, n) \times [0, n))$ and $u_j = u(j/n)$ is the grid data on the regular mesh $\{j/n, j \in \mathbb{G}_n\}$ on D . Note that the evaluation of the coefficients $\widehat{u}_{e,n}$ can be accomplished in $O(N \log N)$, $N = (bn)^2$, operations using FFT. The numerical scheme eq. (6) can be rewritten in the form of a quadrature given by

$$(7) \quad (A_n u)(x) = \sum_{j \in \mathbb{G}_n} w_j^n(x) u(x_j)$$

with quadrature points $x_j = j/n$, and weights

$$(8) \quad w_j^n(x) = \frac{1}{(nb)^2} \sum_{k \in \mathbb{F}_n} \widehat{g}(k) e^{2\pi i k \cdot (x - x_j)/b}, \quad j \in \mathbb{G}_n.$$

2.2. Moments. While eq. (6) provides an $O(N \log N)$ scheme for obtaining the convolution on an equispaced grid of size $N = (bn)^2$, the quadrature eq. (7) with the pre-computed weights can be used to compute $(A_n u)(x)$ for any given x . Use of either form requires that the moment $\widehat{g}(k)$ is available for all $k \in \mathbb{F}_n$. In particular, for a radially symmetric g , that is, $g(y) = g(|y|)$, the calculation of $\widehat{g}(k)$ simplifies as follows

$$(9) \quad \widehat{g}(k) = \int_{B_a(0)} g(y) e^{-2\pi i k \cdot y/b} dy = 2\pi \int_0^a g(\rho) J_0(2\pi|k|\rho/b) \rho d\rho,$$

where the radial integral can be evaluated analytically in several cases of practical interest. For instance, if $g(x) = -\frac{1}{2\pi} \log|x|$ (Laplacian kernel), we have

$$\widehat{g}(k) = \begin{cases} \frac{a^2}{4}(1 - 2 \log a), & |k| = 0, \\ -\frac{a \log a J_1(2\pi|k|a/b)}{2\pi|k|/b} + \frac{1 - J_0(2\pi|k|a/b)}{(2\pi|k|/b)^2}, & |k| \neq 0. \end{cases}$$

Similarly, for $g(x) = \frac{i}{4} H_0^{(1)}(\kappa|x|)$, a kernel of interest for scattering calculations in two dimensions, we have

$$\widehat{g}(k) = 2\pi \int_0^a H_0^{(1)}(\kappa\rho) J_0(2\pi|k|\rho/b) \rho d\rho = \begin{cases} \frac{\pi}{2\kappa} \left(ia J_1(\kappa a) - a Y_1(\kappa a) + \frac{2}{\kappa\pi} \right), & |k| = 0, \\ \frac{i\pi \left(\frac{2\pi|k|a}{b} \right) J_1 \left(\frac{2\pi|k|a}{b} \right) H_0^{(1)}(\kappa a) - \kappa a J_0 \left(\frac{2\pi|k|a}{b} \right) H_1^{(1)}(\kappa a) - \frac{2i}{\pi}}{2(2\pi|k|/b)^2 - \kappa^2}, & \kappa \neq \frac{2\pi|k|}{b}, |k| \neq 0, \\ \frac{i}{4} \pi a^2 \left(J_0(\kappa a) H_0^{(1)}(\kappa a) + J_1(\kappa a) H_1^{(1)}(\kappa a) \right), & \kappa = \frac{2\pi|k|}{b}, |k| \neq 0. \end{cases}$$

For $g(x) = (2\pi|x|)^{-1}$, the values for $\widehat{g}(k)$ is given by the expression

$$\begin{cases} a, & |k| = 0, \\ a \left(J_0 \left(\frac{2\pi|k|a}{b} \right) + \frac{\pi}{2} \left(J_1 \left(\frac{2\pi|k|a}{b} \right) \mathbf{H}_0 \left(\frac{2\pi|k|a}{b} \right) - J_0 \left(\frac{2\pi|k|a}{b} \right) \mathbf{H}_1 \left(\frac{2\pi|k|a}{b} \right) \right) \right), & |k| \neq 0, \end{cases}$$

where $\mathbf{H}_\nu(x)$ denotes the Struve function of order ν . The corresponding expression for $g(x) = \frac{1}{2\pi}|x|^{-1/2}$ reads

$$\begin{cases} \frac{2}{3} a^{3/2}, & |k| = 0, \\ \frac{\frac{\sqrt{2}}{(2\pi|k|/b)^{3/2}} \frac{\Gamma(3/4)}{\Gamma(1/4)}}{\frac{a}{(2\pi|k|/b)^{1/2}} \left(\frac{1}{2} J_0 \left(\frac{2\pi|k|a}{b} \right) S_{-1/2,-1} \left(\frac{2\pi|k|a}{b} \right) - J_1 \left(\frac{2\pi|k|a}{b} \right) S_{1/2,0} \left(\frac{2\pi|k|a}{b} \right) \right)}, & |k| \neq 0, \end{cases}$$

where $S_{\mu,\nu}$ are Lommel functions (see [20]). More generally, for $g(x) = \frac{1}{2\pi}|x|^\gamma$, $\gamma > -2$, the corresponding expression is given by

$$\begin{cases} \frac{1}{2+\gamma} a^{2+\gamma}, & |k| = 0, \\ \frac{\frac{2^{1+\gamma}}{(2\pi|k|/b)^{2+\gamma}} \frac{\Gamma(1+\gamma/2)}{\Gamma(-\gamma/2)}}{\frac{a}{(2\pi|k|/b)^{1+\gamma}} \left(\gamma J_0 \left(\frac{2\pi|k|a}{b} \right) S_{\gamma,-1} \left(\frac{2\pi|k|a}{b} \right) + J_1 \left(\frac{2\pi|k|a}{b} \right) S_{1+\gamma,0} \left(\frac{2\pi|k|a}{b} \right) \right)}, & |k| \neq 0. \end{cases}$$

However, for a general weakly singular kernel, an analytic expression for $\widehat{g}(k)$ may not be readily available. In such cases where obtaining exact expression is not possible, we

can numerically pre-compute them with high precision for their later use. The numerical computations of $\widehat{g}(k)$ poses difficulties mainly due to the singularity present in the integrand at $\rho = 0$. We resolve this singularity using a change of variable of the form $\rho = \tau^p$ by choosing a sufficiently large integer $p > 1$. The integrand of resulting integral

$$\widehat{g}(k) = 2\pi p \int_0^{a^{1/p}} g(\tau^p) J_0(2\pi|k|\tau^p/b) \tau^{2p-1} d\tau,$$

has a high degree of smoothness in τ , and therefore, can be computed accurately using a high-order quadrature. For calculations in this paper, we used the Clenshaw-Curtis quadrature where, for integration domain $[0, \alpha]$, with $\alpha > 0$, the quadrature points $\{x_j^{cc} : j = 1, \dots, n_{pc}\}$ and the weights $\{\omega_j^{cc} : j = 1, \dots, n_{pc}\}$ are given by

$$(10) \quad x_j^{cc} = \frac{\alpha}{2} \left(1 + \cos \left(\left(j - \frac{1}{2} \right) \frac{\pi}{n_{pc}} \right) \right),$$

and

$$(11) \quad \omega_j^{cc} = \frac{\alpha}{n_{pc}} \sum_{k=0}^{n_{pc}}{}' \vartheta_k \cos \left(\left(j - \frac{1}{2} \right) \frac{k\pi}{n_{pc}} \right),$$

with

$$\vartheta_k = \begin{cases} -2/(k^2 - 1), & \text{if } k \text{ is even,} \\ 0, & \text{if } k \text{ is odd,} \end{cases}$$

where the primed sum denote that the first term in the summation is halved.

2.3. Localization. In many large calculations, especially when an analytic expression is not available for \widehat{g} , one can reduce the pre-computation time by localizing the singularity in the integral eq. (5) defining $\widehat{g}(k)$ to a small neighborhood of the singularity. Toward this, we start by splitting the integral operator $(Au)(x)$ using a smooth windowing function, say η_β for some $\beta > 0$, with the following properties – (a) $\eta_\beta : [0, \infty) \rightarrow [0, 1]$ is an infinitely differentiable function, (b) $\eta_\beta(|x|) = 0$ for all x with $|x| \geq \beta$ and (c) $\eta_\beta(|x|) = 1$ for all x with $|x| \leq \beta/2$. Indeed, using η_β , the convolution integral in eq. (1) can be split into two integrals as

$$(12) \quad (Au)(x) = \int_D g(x-y)(1 - \eta_\beta(|x-y|))u(y) dy + \int_{B_\beta(x)} g(x-y)\eta_\beta(|x-y|)u(y) dy.$$

The first convolution in eq. (12) with the smooth kernel $g(x)(1 - \eta_\beta(|x|))$ and compactly supported density u is approximated to high-order using the classical trapezoidal rule. Obviously, when this is implemented using the FFT, the computational cost reduces to $O(N \log N)$. The second convolution in eq. (12) with the localized weakly singular kernel $g(x)\eta_\beta(|x|)$ is computed using the numerical integration scheme given in eq. (6), where \widehat{g} is appropriately replaced with

$$\widehat{g}_{\eta_\beta}(k) = \int_{B_\beta(0)} g(y)\eta_\beta(|y|)e^{-2\pi i k \cdot y/b} dy$$

which, for a radially symmetric g , reduces to

$$\widehat{g}_{\eta_\beta}(k) = 2\pi \int_0^\beta g(\rho)\eta_\beta(\rho)J_0(2\pi|k|\rho/b)\rho d\rho.$$

Again, we can pre-compute these localized weights numerically using a high-order quadrature after resolving the singularity through the change of variable $\rho = \tau^p$ for sufficiently large integer $p > 1$. Although we can again employ the quadrature with points and weights given by eq. (10)-eq. (11), however, as the integrand vanishes to a high-order at both endpoints, the use of the classical trapezoidal rule is as accurate and computationally cheaper. Moreover, the relatively smaller integration domain reduces the pre-computation time even further while maintaining the desired accuracy.

2.4. Improved rate of convergence for discontinuous density. While the integration scheme presented in Section 2.1 converges to high-order for smooth and compactly supported density u , it converges with only first-order when u is discontinuous in D . In this section, we explore the Fourier smoothing technique introduced in [6] and further developed in [8, 27], to enhance the convergence rate while maintaining $O(N \log N)$ computational cost. Use of the resulting quadrature rule in the Nyström method for the solution of the Lippmann-Schwinger equation, in turn, produces second-order convergent approximations when material discontinuities are present in the scattering geometry. This enhancement in the convergence rate is a notable improvement as most of the existing fast numerical techniques yield only the first-order convergent solution when we have discontinuity across the material interfaces. We know that the Fourier smoothing also alleviates numerical difficulties that arise due to non-smooth boundaries [6], a property which remains true for the proposed scheme as well, as seen in Example 10 in the next section.

More precisely, we consider the indicator function $\chi_\Omega(x)$ satisfying $\chi_\Omega(x) = 1$ if $x \in \Omega = \{x \mid u(x) \neq 0\} \subsetneq D$, and zero otherwise. Let \tilde{u} be a smooth extension of u such that $\tilde{u}(x) = u(x)$ for all $x \in \Omega$. Now, using \tilde{u} and χ_Ω , we recast the integral operator eq. (1) as

$$(13) \quad (Au)(x) = \int_D g(x-y)\tilde{u}(y)\chi_\Omega(y)\psi(y)dy,$$

where ψ is a smooth window function such that $\psi(x) = 1$ for $x \in \Omega$ and $\psi(x) = 0$ for $x \in \partial D$. For illustration, a specific instance of ψ is depicted in Figure 1. The key idea is to replace χ_Ω in eq. (13) by its truncated Fourier series

$$(14) \quad \chi_\Omega^n(x) = \sum_{k \in \mathbb{F}_n} \widehat{\chi}_\Omega^n(k) e^{2\pi i k \cdot x}.$$

Using the integration scheme A_n , we obtain the approximation to Au as $A_n(\tilde{u}\chi_\Omega^n\psi)$, that converges with second-order provided Fourier coefficients $\widehat{\chi}_\Omega^n(k)$ are known accurately either numerically or analytically. A partial mathematical justification for the second-order convergence by means of this Fourier smoothing technique can be found in [7, 23].

3. NUMERICAL EXAMPLES

As we have mentioned in the introduction, this paper aims twofold: first, to design a fast high order integration scheme to approximate convolution integral eq. (1), and second, its application to the solution of constant linear coefficient partial differential equations and Lippmann-Schwinger integral equation. First, in Section 3.1, we illustrate our integration

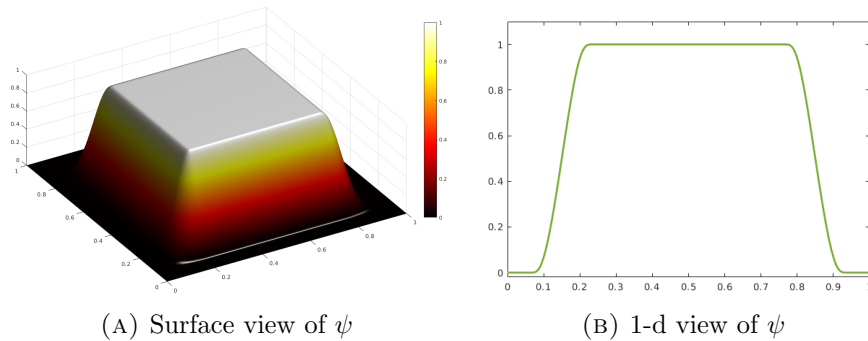


FIGURE 1. Smooth vanishing window function ψ .

scheme's high order character and performance for various weakly singular kernels with different degrees of smoothness in the extended density u_e . Subsequently, in Section 3.2 and Section 3.3, we present simulation results for certain partial differential equations and the Lippmann-Schwinger equation.

The relative error reported in all the examples are computed as

$$(15) \quad \varepsilon_n = \frac{\max_{j \in G_n} |(\mathbf{U}_{\text{exact}})(j/n) - (\mathbf{U}_{\text{approx}})(j/n)|}{\max_{j \in G_n} |(\mathbf{U}_{\text{exact}})(j/n)|},$$

where $\mathbf{U}_{\text{approx}}$ and $\mathbf{U}_{\text{exact}}$ (either obtained analytically or computed by our scheme at a very fine grid) denote the approximate and exact values of the quantity to be computed, respectively. In the formula eq. (15), subscript n stands for the number of grid points in each dimension. The numerical order of convergence (noc), which relates to the rate at which the accuracy of the approximation improves as n increases, is computed by the following formula:

$$(16) \quad \text{noc} = \log_2 \left(\frac{\varepsilon_n}{\varepsilon_{2n}} \right).$$

For all experiments in this section, we have taken the extended computational domain $D_e = [0, b]^2$ with $b = 3$, the smallest integer greater than $1 + \sqrt{2}$.

3.1. Approximation of the convolution integral.

In this section, we demonstrate the performance (convergence rate and computational complexity) of the proposed integration scheme for approximation of the convolution integral eq. (1) through a variety of examples.

Example 1. (*Super-algebraic convergence*) In this example, we demonstrate the performance of our numerical integration scheme for infinitely smooth compactly supported density for several weakly singular kernels. We obtain numerical approximations of eq. (1) for four different singular kernels, namely, $g(x) = |x|^\gamma$, $\gamma = -1/2, -1, -3/2$, and $g(x) = \log(|x|)$ with density

$$(17) \quad u(y) = (1/2\pi\sigma^2) \exp(-(|y|^2/2\sigma^2)),$$

where $\sigma = 0.05$. The results are presented in table 1 which clearly corroborates the super algebraic convergence of the proposed algorithm for infinitely smooth and compactly supported densities.

n	$g(x) = x ^{-1/2}$		$g(x) = x ^{-1}$		$g(x) = x ^{-3/2}$		$g(x) = \log(x)$	
	ε_n	noc	ε_n	noc	ε_n	noc	ε_n	noc
2^2	1.7×10^0	—	8.9×10^{-1}	—	3.9×10^{-1}	—	2.4×10^0	—
2^3	2.3×10^{-1}	3.1	1.8×10^{-1}	2.6	1.1×10^{-1}	2.0	2.3×10^{-1}	3.6
2^4	2.7×10^{-3}	6.4	1.7×10^{-3}	6.7	1.7×10^{-3}	6.0	1.3×10^{-3}	7.5
2^5	1.6×10^{-7}	14.0	1.1×10^{-8}	17.3	1.5×10^{-8}	16.8	3.8×10^{-9}	18.4
2^6	5.3×10^{-15}	24.9	2.9×10^{-16}	25.1	6.6×10^{-16}	24.4	2.5×10^{-15}	20.5

TABLE 1. Convergence study: Super algebraic convergence for a set of different weakly singular kernels with infinitely smooth compactly supported function $u(y) = (1/2\pi\sigma^2) \exp(-|y|^2/2\sigma^2)$ with $\sigma = 0.05$.

To numerically validate the computational complexity of our algorithm, in Figure 2, we have plotted the computational time (required for obtaining $(A_n u)(x_j)$, for all $j \in \mathbb{G}_n$) against the total number of grid points $N = (bn)^2$ for $n = 24\ell$, $\ell = 1, \dots, 21$. For this simulation, we have taken $g(x) = \log|x|$ with the Gaussian density u defined in eq. (17). The plot shows that the computational time indeed behaves as $CN \log N$, where $C = 1.2 \times 10^{-7}$, which confirms the expected $O(N \log N)$ complexity of the proposed integration scheme.

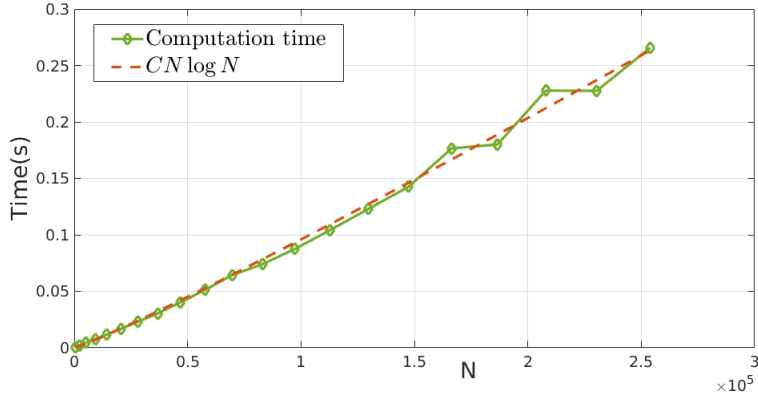


FIGURE 2. The Computation time for the integration scheme against $N = (bn)^2$. For comparison, a reference curve $C(N \log N)$ with $C = 1.2 \times 10^{-7}$ is also shown.

Example 2. (*The rate of convergence*) The error in our integration scheme depends on the asymptotic behaviour of $|\hat{g}(k)|$ and $|\hat{u}_e(k)|$ (given in eq. (5)). To explore these dependence, we include two different sets of experiments. In the first group of simulations, numerical approximations of eq. (1) are obtained for a fixed density $u(x) = (x_1(1-x_1)x_2(1-x_2))^3$ with the same four kernels used in Example 1. The corresponding convergence results are displayed in Table 2.

In our second set of experiments, we take $g(x) = |x|^{-1}$ and compute the approximations of eq. (1) for four different densities $u(x) = (x_1(1-x_1)x_2(1-x_2))^m$, $m = 1, 2, 3, 4$ and the

n	$g(x) = x ^{-1/2}$		$g(x) = x ^{-1}$		$g(x) = x ^{-3/2}$		$g(x) = \log(x)$	
	ε_n	noc	ε_n	noc	ε_n	noc	ε_n	noc
2^2	2.2×10^{-2}	—	6.8×10^{-3}	—	4.9×10^{-3}	—	8.2×10^{-3}	—
2^3	8.0×10^{-4}	4.8	6.1×10^{-4}	3.5	4.9×10^{-4}	3.3	4.8×10^{-4}	4.1
2^4	4.7×10^{-5}	4.1	4.7×10^{-5}	3.7	4.8×10^{-5}	3.3	3.1×10^{-5}	4.0
2^5	3.1×10^{-6}	4.0	3.4×10^{-6}	3.8	4.6×10^{-6}	3.4	1.9×10^{-6}	4.0
2^6	1.9×10^{-7}	4.0	2.4×10^{-7}	3.8	4.2×10^{-7}	3.4	1.2×10^{-7}	4.0
2^7	1.2×10^{-8}	4.0	1.7×10^{-8}	3.8	3.8×10^{-8}	3.5	7.4×10^{-9}	4.0
2^8	7.6×10^{-10}	4.0	1.2×10^{-9}	3.9	3.4×10^{-9}	3.5	4.6×10^{-10}	4.0

TABLE 2. An experiment to study the effect of g on the convergence rate: Convolutions with different kernels and fixed density $u(x) = (x_1(1-x_1)x_2(1-x_2))^3$.

n	m = 1		m = 2		m = 3		m = 4	
	ε_n	noc	ε_n	noc	ε_n	noc	ε_n	noc
2^3	1.4×10^{-2}	—	2.6×10^{-4}	—	6.1×10^{-4}	—	1.0×10^{-4}	—
2^4	4.2×10^{-3}	1.8	4.2×10^{-5}	2.6	4.7×10^{-5}	3.7	2.0×10^{-6}	5.7
2^5	1.2×10^{-3}	1.8	5.9×10^{-6}	2.8	3.4×10^{-6}	3.8	7.6×10^{-8}	4.7
2^6	3.4×10^{-4}	1.8	7.9×10^{-7}	2.9	2.4×10^{-7}	3.8	2.6×10^{-9}	4.9
2^7	9.4×10^{-5}	1.9	1.0×10^{-7}	3.0	1.7×10^{-8}	3.8	8.5×10^{-11}	4.9
2^8	2.6×10^{-5}	1.9	1.3×10^{-8}	3.0	1.2×10^{-9}	3.9	2.7×10^{-12}	5.0
2^9	7.1×10^{-6}	1.9	1.7×10^{-9}	3.0	7.9×10^{-11}	3.9	8.7×10^{-14}	5.0

TABLE 3. An experiment to study the impact of smoothness of u_e on the convergence rate: Convolution with fixed kernel $g(x) = |x|^{-1}$ and densities $u(x) = (x_1(1-x_1)x_2(1-x_2))^m$, $m = 1, 2, 3, 4$.

corresponding results are reported in table 3. We see that, with increasing smoothness of u_e as m increases, the corresponding rate of convergence improves proportionally.

Example 3. (*Performance comparison of localized and non-localized schemes*) As discussed in Section 2.3, in absence of any analytical formula for obtaining the moments $|\widehat{g}(k)|$, they can be precomputed rapidly to a high degree of accuracy using the localization technique. In this example, to compare the computational times of local and non-local schemes, we compute the convolution integral eq. (1) with $g(x) = \log |x|$ and $u(x) = (x_1(1-x_1)x_2(1-x_2))^3$ using both methods for several values of n . We choose an optimal value for n_{pc} in the pre-computation of localized as well as non-localized moments in such a way that the respective approximations have comparable accuracy level as the one obtained using the analytic expression for $|\widehat{g}(k)|$ given in Section 2.2. The respective computational times are displayed in Figure 3(a) and

the corresponding error are shown in Figure 3(b). We see that, due to the reduced pre-computation cost for the localized integration, there is a significant improvement in the overall computation time as compared to the non-local scheme.

Next, to confirm that there is no loss of accuracy in the local scheme compared to the one without localization, we repeat the experiments done in example 2 with localized moments obtained numerically. The corresponding errors are reported in table 4 and table 5. We see that the accuracy levels and convergence behaviour are nearly identical to those seen in table 2 and table 3, respectively.

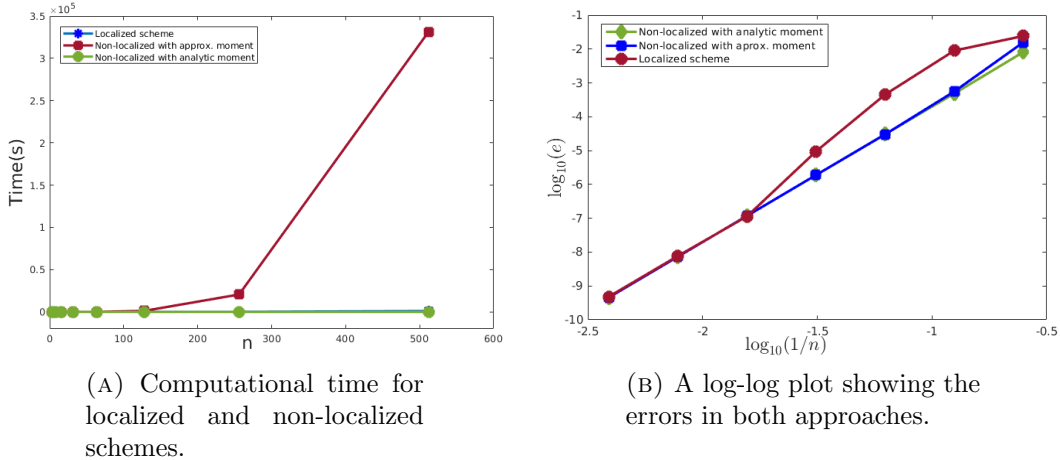


FIGURE 3. A comparison of total computational time for localized and non-localized schemes for computing the convolution with $g(x) = \log(|x|)$ and $u(x) = (x_1(1-x_1)x_2(1-x_2))^3$: The experiment indicate a significant improvement in the computational time for the localized scheme while maintaining the same degree of accuracy in the approximation.

Example 4. (*A kernel that is not radially symmetric*) As the final example of this section, we take the kernel

$$g(x) = -\frac{1}{2\pi} \frac{x_1}{x_1^2 + x_2^2}$$

to demonstrate that the proposed method is not limited to only radially symmetric kernels. We compute the approximations of eq. (1) for four different densities. As the first experiment, we take

$$u(x) = 4\alpha(\alpha|x-c|^2 - 1) \exp(-\alpha|x-c|^2)$$

with $\alpha = 250$ and $c = (1/2, 1/2)$ and compare the numerical approximations with the exact value

$$(Au)(x) = -2\alpha(x_1 - c_1) \exp(-\alpha|x-c|^2).$$

The results reported in the two leftmost columns labeled “Gaussian” in Table 6 confirms the exponential convergence. Next, we take the density

$$u(x) = \Delta((x_1(1-x_1)x_2(1-x_2))^m),$$

for $m = 4, 5, 6$, and compare the approximations with the exact convolution

$$(Au)(x) = -m(2x_1 - 1)(x_1(1 - x_1))^{m-1}(x_2(1 - x_2))^m, \quad m = 4, 5, 6.$$

The errors and corresponding numerical order of convergence are reported in Table 6.

3.2. Numerical solution of partial differential equations. It is known that if g is a fundamental solution of the linear constant-coefficient partial differential operator L , then

$$v(x) = \int_{\mathbb{R}^2} g(x - y)f(y) dy, \quad x \in \mathbb{R}^2,$$

solves $Lv = f$ in \mathbb{R}^2 provided $f \in L^1(\mathbb{R}^2)$. Some important examples include $L = -\Delta$, $L = -\Delta + \kappa^2 I$, and $L = \Delta + \kappa^2 I$, where I is the identity operator. Thus, if the source distribution f is compactly supported, say in D , then the proposed integration scheme can be utilized to compute the solution to $Lv = f$.

Example 5. We consider the Poisson equation

$$(18) \quad -\Delta u(x) = f(x),$$

where the corresponding fundamental solution is given by $g(x) = -\frac{1}{2\pi} \log |x|$. For

$$f(x) = \sum_{i=1}^{\ell} (4\alpha^2 |x - c_i|^2 - 4\alpha) \exp(-\alpha |x - c_i|^2),$$

the exact solution is given by

$$u(x) = \sum_{i=1}^{\ell} \exp(-\alpha |x - c_i|^2).$$

We compute the solution for $\alpha = 250$ and $\ell = 3$, where $c_1 = (0.6, 0.6)$, $c_2 = (0.5, 0.5)$, and $c_3 = (0.35, 0.6)$. The results are given in table 7, where we clearly see a super-algebraic convergence. A similar convergence study is also included in table 7 for $\alpha = 950$ and

n	$g(x) = x ^{-1/2}$		$g(x) = x ^{-1}$		$g(x) = x ^{-3/2}$		$g(x) = \log(x)$	
	ε_n	noc	ε_n	noc	ε_n	noc	ε_n	noc
2^2	7.6×10^{-2}	—	3.3×10^{-2}	—	5.2×10^{-3}	—	2.4×10^{-2}	—
2^3	4.6×10^{-3}	4.0	4.1×10^{-3}	3.0	4.9×10^{-4}	3.1	9.0×10^{-3}	1.5
2^4	8.8×10^{-5}	5.7	2.0×10^{-4}	4.3	4.9×10^{-5}	3.6	4.5×10^{-4}	4.3
2^5	3.5×10^{-6}	4.7	5.4×10^{-6}	5.2	5.1×10^{-6}	3.2	9.5×10^{-6}	5.6
2^6	2.3×10^{-7}	3.9	3.4×10^{-7}	4.0	4.8×10^{-7}	3.4	1.1×10^{-7}	6.4
2^7	1.4×10^{-8}	4.0	2.7×10^{-8}	3.7	4.5×10^{-8}	3.4	7.7×10^{-9}	3.9
2^8	9.0×10^{-10}	4.0	1.9×10^{-9}	3.8	4.0×10^{-9}	3.5	4.8×10^{-10}	4.0

TABLE 4. An experiment to study the impact of g on the convergence rate of the localized scheme: Convolution with various kernels and fixed density $u(x) = (x_1(1 - x_1)x_2(1 - x_2))^3$.

	$m = 1$		$m = 2$		$m = 3$		$m = 4$	
n	ε_n	noc	ε_n	noc	ε_n	noc	ε_n	noc
2^2	6.0×10^{-2}	—	2.0×10^{-2}	—	3.3×10^{-2}	—	9.1×10^{-3}	—
2^3	1.5×10^{-2}	2.0	4.6×10^{-3}	2.1	4.1×10^{-3}	3.0	1.1×10^{-3}	3.0
2^4	5.1×10^{-3}	1.6	2.4×10^{-4}	4.3	2.0×10^{-4}	4.3	1.7×10^{-5}	6.0
2^5	1.6×10^{-3}	1.7	1.4×10^{-5}	4.1	5.4×10^{-6}	5.2	2.6×10^{-7}	6.1
2^6	4.7×10^{-4}	1.7	1.5×10^{-6}	3.2	3.4×10^{-7}	4.0	3.5×10^{-9}	6.3
2^7	1.4×10^{-4}	1.8	1.9×10^{-7}	2.9	2.7×10^{-8}	3.7	1.2×10^{-10}	4.8
2^8	3.9×10^{-5}	1.8	2.4×10^{-8}	3.0	1.9×10^{-9}	3.8	4.0×10^{-12}	5.0

TABLE 5. An experiment to study the impact of smoothness of u_e on the convergence rate of the localized scheme: Convolution with $g(x) = |x|^{-1}$ and $u(x) = (x_1(1-x_1)x_2(1-x_2))^m$, $m = 1, 2, 3, 4$.

$\ell = 10$ with $c_1 = (0.6, 0.6)$, $c_2 = (0.5, 0.5)$, $c_3 = (0.35, 0.6)$, $c_4 = (0.6, 0.8)$, $c_5 = (0.8, 0.8)$, $c_6 = (0.25, 0.5)$, $c_7 = (0.75, 0.5)$, $c_8 = (0.25, 0.25)$, $c_9 = (0.5, 0.25)$, and $c_{10} = (0.75, 0.25)$. The corresponding solutions are shown in fig. 4.

We next consider $\Delta u = f$ with a discontinuous right hand side. More precisely, we take

$$(19) \quad f(x) = \begin{cases} 1, & x \in [0.3, 0.7]^2 \\ 0, & x \in D \setminus [0.3, 0.7]^2. \end{cases}$$

In this case, we compare the solutions obtained using the integration scheme with and without Fourier smoothing. The results presented in table 8 demonstrate a significant improvement in the accuracy and enhancement in convergence rate for the Fourier smoothed

	Gaussian		$m = 4$		$m = 5$		$m = 6$	
n	ε_n	noc	ε_n	noc	ε_n	noc	ε_n	noc
2^2	—	—	8.1×10^{-2}	—	3.4×10^{-1}	—	5.3×10^{-1}	—
2^3	$2.0 \times 10^{+1}$	—	2.4×10^{-2}	1.8	1.4×10^{-2}	4.3	3.6×10^{-3}	6.6
2^4	1.6×10^{-1}	3.8	3.2×10^{-3}	2.7	7.1×10^{-4}	4.2	2.7×10^{-4}	3.7
2^5	6.2×10^{-5}	11.3	4.3×10^{-4}	2.9	4.3×10^{-5}	4.0	1.0×10^{-5}	4.7
2^6	2.7×10^{-16}	37.6	5.5×10^{-5}	3.0	2.6×10^{-6}	4.0	3.3×10^{-7}	4.9
2^7	—	—	7.0×10^{-6}	3.0	1.6×10^{-7}	4.0	1.1×10^{-8}	5.0
2^8	—	—	8.8×10^{-7}	3.0	1.0×10^{-8}	4.0	3.3×10^{-10}	5.0

TABLE 6. A convergence study for a non-radial weakly singular kernel: The convolution integral with $g(x) = -x_1/(2\pi(x_1^2+x_2^2))$ and the ‘‘Gaussian’’ $u(x) = 4\alpha(\alpha|x-c|^2-1)\exp(-\alpha|x-c|^2)$ with $\alpha = 250$ and $c = (0.5, 0.5)$, and $u(x) = \Delta((x_1(1-x_1)x_2(1-x_2))^m)$, $m = 4, 5, 6$.

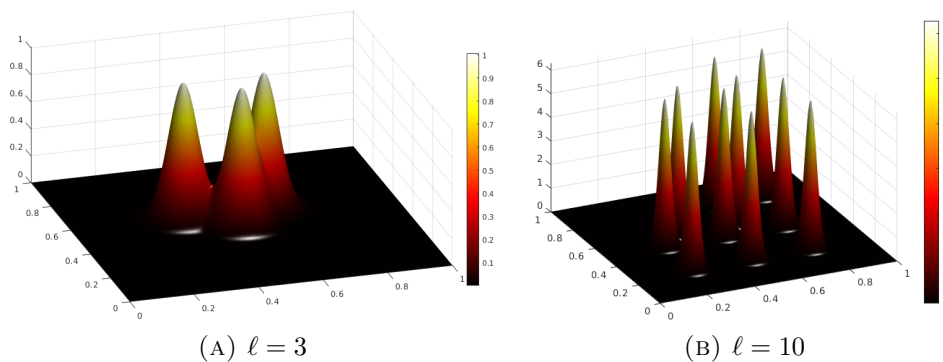


FIGURE 4. Solution to the Poisson equation

$\ell = 3$			$\ell = 10$		
n	ε_n	noc	n	ε_n	noc
2^2	2.2×10^{01}	—	2^3	8.59×10^{01}	—
2^3	7.1×10^{00}	1.6	2^4	1.47×10^{01}	2.6
2^4	5.6×10^{-02}	7.0	2^5	6.3×10^{-02}	7.9
2^5	2.8×10^{-06}	14.3	2^6	1.4×10^{-06}	15.5
2^6	9.7×10^{-14}	24.8	2^7	2.9×10^{-15}	28.5

TABLE 7. A convergence study for the Poisson problem in Example 5.

n	WFS		FS	
	ε_n	noc	ε_n	noc
2^2	3.6×10^{-1}	—	7.9×10^{-2}	—
2^3	1.9×10^{-1}	1.17	2.8×10^{-3}	4.79
2^4	7.2×10^{-2}	1.33	5.3×10^{-4}	2.42
2^5	3.7×10^{-2}	0.92	8.9×10^{-5}	2.57
2^6	2.0×10^{-2}	0.91	2.1×10^{-5}	2.07
2^7	9.9×10^{-3}	1.02	5.2×10^{-6}	2.04
2^8	4.9×10^{-3}	1.02	1.3×10^{-6}	2.02

TABLE 8. A comparison between the Fourier smoothed (FS), and without Fourier smoothed (WFS) versions of the scheme for the discontinuous density given in eq. (19).

scheme. For instance, for $n = 256$, the result obtained from the Fourier smoothed version of the scheme is more than three thousand times accurate in comparison to that obtained without Fourier smoothing.

$\kappa = 1$			$\kappa = 200$		
n	ε_n	noc	n	ε_n	noc
2^2	1.5×10^{01}	—	2^2	1.3×10^{-02}	—
2^3	2.1×10^{00}	02.9	2^3	6.1×10^{-03}	01.1
2^4	5.4×10^{-03}	08.6	2^4	2.2×10^{-04}	04.8
2^5	3.2×10^{-09}	20.7	2^5	6.0×10^{-10}	18.5
2^6	6.7×10^{-16}	22.2	2^6	2.3×10^{-16}	21.3

TABLE 9. Convergence study for the solution of eq. (20) with density f given in eq. (21).

Example 6. Next, we consider the equation

$$(20) \quad -\Delta u(x) + \kappa^2 u(x) = f(x),$$

with the fundamental solution $g(x) = \frac{1}{2\pi} K_0(\kappa|x|)$, where K_0 is the modified Bessel function of the second kind of order 0. For

$$(21) \quad f(x) = \left(\frac{-4|x|^2 + 4\delta^2}{\delta^4} + \kappa^2 \right) \exp\left(-\frac{1}{\delta^2}|x|^2\right),$$

the exact solution is given by

$$u(x) = \exp\left(-\frac{1}{\delta^2}|x|^2\right).$$

The corresponding computational results for $\delta = 0.08$ are shown in table 9, where we again observe the super algebraic convergence.

3.3. Application to the volumetric scattering problem. In this section, utilizing our integration scheme, we design a fast and accurate Nyström solver for the problem of wave scattering by penetrable inhomogeneous media. This solver converges super algebraically when the material properties are smooth. In addition, our algorithm converges with second-order using the Fourier smoothing technique discussed in Section 2.4 when discontinuous material interfaces are present. Moreover, this quadratic rate of convergence is not constrained by the smoothness of scattering geometry, and the method yields second-order convergence even for obstacles with non-smooth boundaries.

Formally, the problem of scattering of time-harmonic acoustic waves by a bounded inhomogeneity $\Omega \subset \mathbb{R}^2$ can be described as follows: for a given incident wave u^{inc} satisfying the free space Helmholtz equation

$$(22) \quad \Delta u^{inc}(x) + \kappa^2 u^{inc}(x) = 0 \quad x \in \mathbb{R}^2,$$

find the total field u such that [13]

$$(23) \quad \Delta u(x) + \kappa^2 \mu(x) u(x) = 0, \quad x \in \mathbb{R}^2,$$

and scattered field $u^{sc} = u - u^{inc}$ satisfying the Sommerfeld radiation condition [13]

$$(24) \quad \lim_{r \rightarrow \infty} r^{1/2} \left(\frac{\partial u^{sc}}{\partial r} - i\kappa u^{sc} \right) = 0,$$

where κ is the wave number of u^{inc} , and $r = |x|$ for $x \in \mathbb{R}^2$. Here, $\mu(x)$ denotes the refractive index of the inhomogeneity that is assumed to be smooth within Ω and takes the value one outside Ω . Moreover, μ is allowed to have a jump discontinuity across the material interface $\partial\Omega$.

An equivalent integral equation formulation of the scattering problem eqs. (22) to (24) is given by the Lippmann-Schwinger equation [13, 26]

$$(25) \quad u(x) + \kappa^2(A(mu))(x) = u^{inc}(x), \quad x \in \Omega,$$

where

$$(26) \quad (Av)(x) = \int_{\Omega} g_{\kappa}(x-y)v(y)dy$$

with the contrast function $m(x) = 1 - \mu(x)$ and $g_{\kappa}(x) = \frac{i}{4}H_0^{(1)}(\kappa|x|)$. Without loss of generality, we take $\Omega \subseteq D$.

An application of eq. (6) at the Nyström nodes $x_j = j/n$, $j \in \mathbb{G}_n$ for approximating $A(mu)$ in eq. (25) yields the following linear system

$$(27) \quad u(x_j) + \kappa^2(A_n(mu))(x_j) = u^{inc}(x_j), \quad j \in \mathbb{G}_n.$$

Finally, the solution of the linear system eq. (27) is obtained using the matrix-free implementation of GMRES in $O(N \log N)$ cost per iterations.

In the next few examples, we present a variety of scattering calculations using our solver. In all the reported experiments, the incident wave is taken as $u^{inc}(x) = e^{i\kappa x_1}$.

Example 7. (*Scattering by a disc with smooth material properties*) As a first exercise of this section, we compute numerical solution of the Lippmann-Schwinger equation eq. (25) over inhomogeneous circular region with acoustical size $\kappa a = 1$, where a denotes the diameter of the inhomogeneity Ω . The refractive index of the inhomogeneous region is given by

$$(28) \quad \mu(x) = \begin{cases} 2, & |x - x_c| \leq t_0, \\ 1 + \varkappa\left(\frac{|x-x_c|-t_0}{t_1-t_0}\right), & t_0 < |x - x_c| < t_1, \\ 1, & \text{otherwise,} \end{cases}$$

where

$$(29) \quad \varkappa(t) = \exp\left(\frac{2e^{-1/t}}{t-1}\right)$$

with $t_1 = 0.45$, $t_0 = 0.9t_1$ and $x_c = (1/2, 1/2)$. For a pictorial visualization of the contrast function, we display a plot of $1 - \mu(x)$ in fig. 5(a). To study the convergence, numerical solution of eq. (25) is computed for several level of discretization and the errors are reported in Table 10. The errors from a similar experiment where $\kappa a = 50$ is also reported in Table 10. The results clearly show the high-order character of our algorithm when the contrast function $1 - \mu$ is smooth and compactly supported. A plot of the absolute value of the total field for a disc of acoustical size $\kappa a = 80$ is displayed in fig. 5(b).

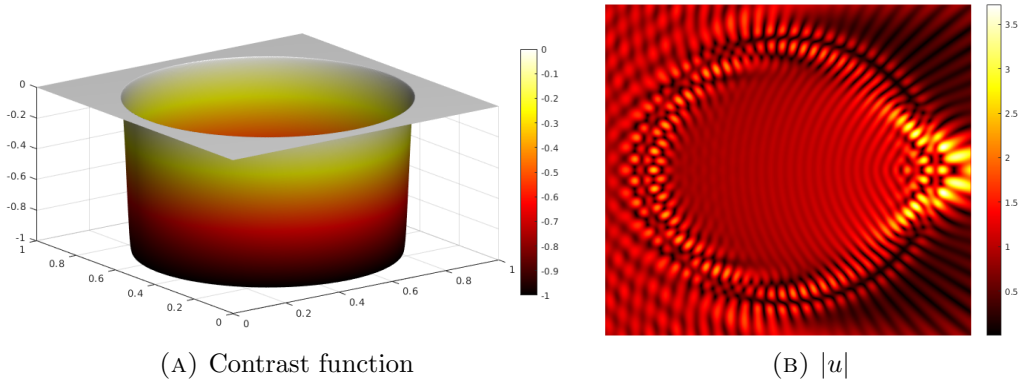


FIGURE 5. (left) The contrast function $1 - \mu(x)$ with refractive index μ given in equation eq. (28). (right) Solution to the scattering problem in Example 7 for the circular disc of size $\kappa a = 80$.

$\kappa a = 1$			$\kappa a = 50$		
n	ε_n	noc	n	ε_n	noc
2^5	2.0×10^{-4}	--	2^5	3.5×10^{-1}	--
2^6	4.1×10^{-5}	2.3	2^6	2.5×10^{-2}	3.8
2^7	7.5×10^{-7}	5.8	2^7	3.8×10^{-4}	5.9
2^8	1.2×10^{-8}	6.0	2^8	4.0×10^{-6}	6.5
2^9	4.6×10^{-11}	8.1	2^9	1.2×10^{-8}	8.4

TABLE 10. Convergence study: plane wave scattering by a circular inhomogeneity with refractive index given in eq. (28).

Example 8. (*Scattering by a smooth filter disc*) In this example, we consider a filter flat disk of diameter $a = 0.5$ with center $x_c = (1/2, 1/2)$ for which the $m(x)$ is given by [29]

$$(30) \quad m(x) = -\exp\left(\frac{-1}{2} \left(\frac{2|x - x_c|}{a}\right)^8\right).$$

A surface visualisation of the contrast function is shown in fig. 6(a). In table 11, we show the errors and the corresponding numerical order of convergence for $\kappa a = 2\pi, 40\pi, 80\pi$. The results again show the super algebraic convergence. For a pictorial visualization, we display a surface plot of the real part of the computed total field for $\kappa a = 80\pi$ in fig. 7(a). For this simulation, we use $n = 4096$.

Example 9. (*Scattering by Luneburg lens*) Next, we consider the nonsmooth Luneburg lens of diameter $a = 0.9$, which is designed to focus an incoming wave to a single point. The $m(x)$ for the Luneburg lens is given by [29]

$$(31) \quad m(x) = \left(\frac{2|x - x_c|}{a}\right)^2 - 1,$$

	$\kappa a = 2\pi$		$\kappa a = 40\pi$		$\kappa a = 80\pi$	
n	ε_n	noc	ε_n	noc	ε_n	noc
2^4	4.7×10^{-4}	—	—	—	—	—
2^5	7.6×10^{-7}	9.3	1.0×10^0	—	—	—
2^6	2.6×10^{-11}	14.8	1.4×10^{-2}	6.2	1.2×10^0	—
2^7	2.6×10^{-14}	10.0	7.9×10^{-12}	30.7	2.8×10^{-4}	12.0
2^8	—	—	8.6×10^{-13}	3.2	1.6×10^{-12}	27.4

TABLE 11. A convergence study for the scattering by smooth filter disc in Example 8.

	$\kappa a = 2\pi$		$\kappa a = 40\pi$		$\kappa a = 80\pi$	
n	ε_n	noc	ε_n	noc	ε_n	noc
2^6	4.8×10^{-5}	—	6.5×10^{-3}	—	9.3×10^{-1}	—
2^7	2.2×10^{-5}	1.1	1.1×10^{-3}	2.5	4.1×10^{-3}	7.8
2^8	2.9×10^{-6}	2.9	1.3×10^{-4}	3.1	3.7×10^{-4}	3.5
2^9	1.8×10^{-7}	4.0	3.8×10^{-5}	1.8	8.7×10^{-5}	2.1
2^{10}	6.6×10^{-8}	1.5	4.5×10^{-6}	3.1	7.0×10^{-6}	3.6

TABLE 12. A convergence study for the scattering by Luneburg lens in Example 9.

where $x_c = (1/2, 1/2)$. The corresponding contrast function is shown in fig. 6(b). In table 12, we present the computational errors for $\kappa a = 2\pi, 40\pi, 80\pi$. We display the real part of the total field computed on the 4096×4096 grid for $\kappa a = 108\pi$ in fig. 7(b).

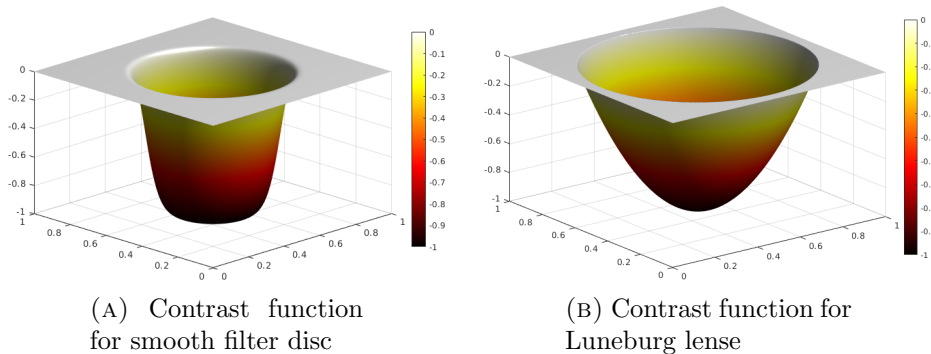


FIGURE 6. A three dimensional view of the contrast function $m(x)$ for the smooth filter disc and the Luneburg lens defined in eq. (30) and eq. (31), respectively.

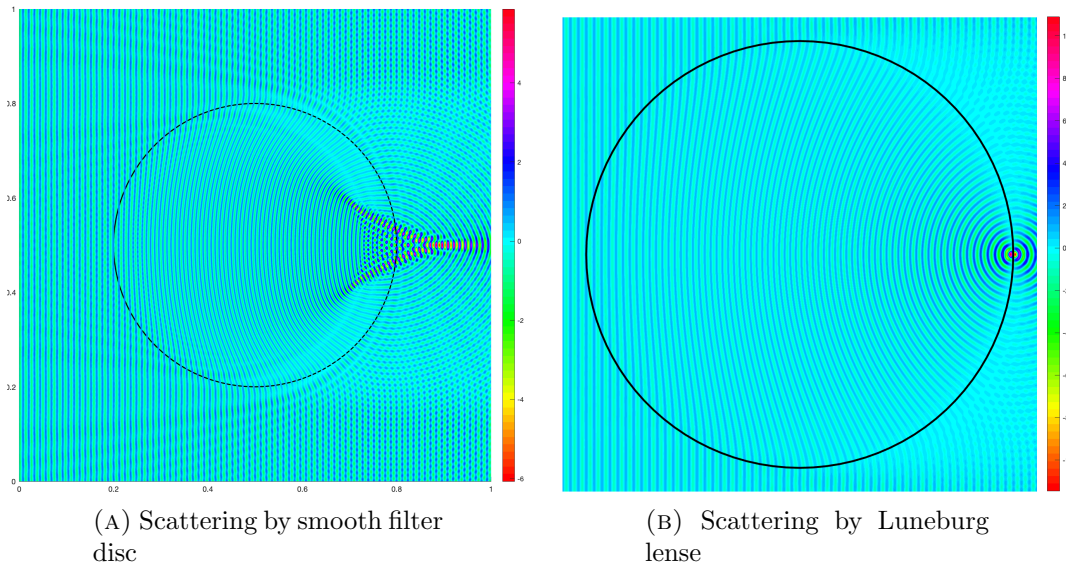


FIGURE 7. (left) Scattering of a plane wave by penetrable smooth filter disc of acoustic size $\kappa a = 80\pi$ in a unit square of size 160π . (right) Scattering of a plane wave by penetrable Luneburg lens of acoustic size $\kappa a = 108\pi$ in a unit square of size 120π . A computational grid of size $n \times n$ with $n = 4096$ is used.

Example 10. (*Scattering in the presence of a discontinuous material interface and Fourier smoothing*) We now consider some examples where the use of Fourier smoothing has beneficial effect on the rate of convergence of the scattering solver. In particular, through these experiments, we compare the solutions obtained by the Nyström solver with and without Fourier smoothing.

First, we consider the disc of acoustic size $\kappa a = 40$ with $m(x) = -1$ in the disc and zero outside. A convergence study is shown in table 13. We observe a significant improvement in the accuracy and enhancement in the convergence rate for the Fourier smoothed version of the method.

Finally, to show that the Fourier smoothing technique is not limited to only simple scattering configurations, we consider a star-shaped geometry containing cusps and a square cavity with corners. In table 13 and table 14, we present a numerical convergence study where the acoustic size of the problem is $\kappa a = 60$ and $\kappa a = 64$, respectively. The absolute value of total and scattered fields are displayed in fig. 8 and fig. 9, where the simulation for the star-shaped geometry uses $\kappa a = 100$ whereas $\kappa a = 128$ in the scattering calculation for the square with a cavity.

4. CONCLUDING DISCUSSION AND FUTURE DIRECTIONS

In this article, we present a simple, efficient, and high-order numerical integration scheme to evaluate convolution integrals of the form

$$(Au)(x) = \int_D g(x-y)u(y) dy,$$

	Disc shape scatterer				Scatterer with cusp	
	WFS		FS		FS	
n	ε_n	noc	ε_n	noc	ε_n	noc
2^4	2.4×10^0	—	2.4×10^0	—	—	—
2^5	2.1×10^0	0.2	7.0×10^{-1}	1.8	9.3×10^{-1}	—
2^6	5.0×10^{-1}	2.1	1.7×10^{-2}	5.4	6.5×10^{-2}	3.9
2^7	2.0×10^{-1}	1.3	3.6×10^{-3}	2.2	5.3×10^{-3}	3.6
2^8	4.7×10^{-2}	2.0	1.1×10^{-3}	1.7	1.2×10^{-3}	2.2
2^9	1.7×10^{-2}	1.5	2.8×10^{-4}	2.0	2.6×10^{-4}	2.2
2^{10}	4.0×10^{-3}	2.0	6.9×10^{-5}	2.0	5.8×10^{-5}	2.1

TABLE 13. A convergence study for the scattering by a disc with $\kappa a = 40$ and by a geometry with non-smooth boundary of size $ka = 60$. The refractive index $\mu(x)$ is discontinuous across the scattering interface.

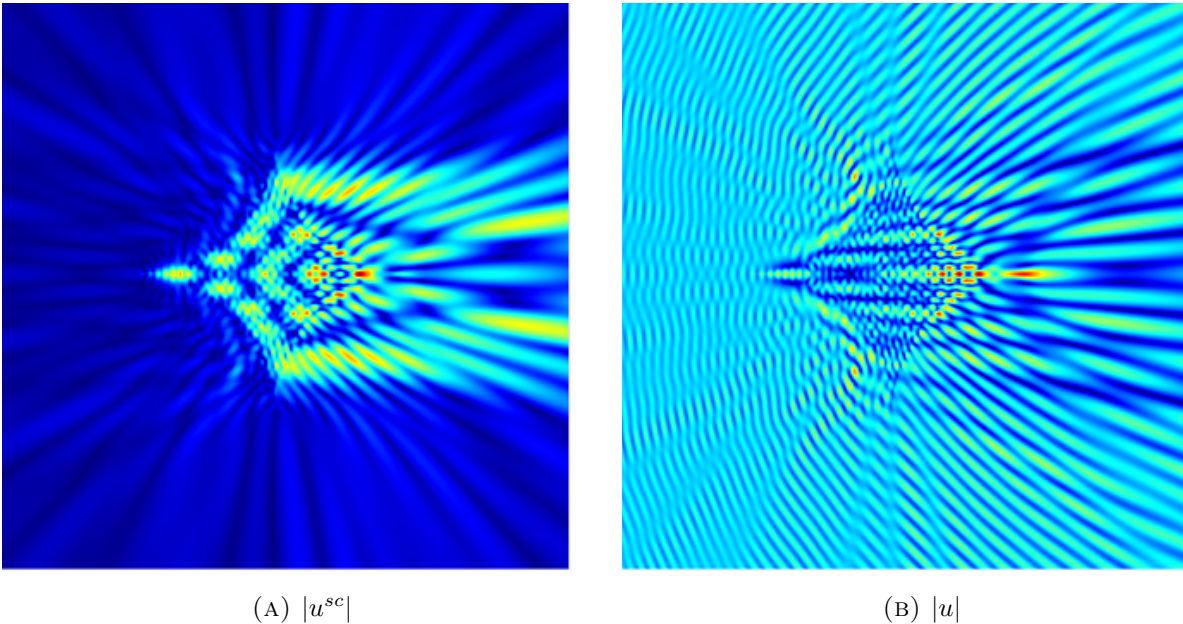


FIGURE 8. Scattering of a plane wave by penetrable inhomogeneity with cusps of acoustic size $\kappa a = 100$, where $\mu(x)$ is discontinuous across the interface. For this simulation, a computational grid of size $n \times n$ with $n = 512$ is used.

where g is weakly singular and u is supported in D . The preeminent motivation for this numerical integration scheme is to compute the convolution Au on a uniform grid of size N in $O(N \log N)$ operations with high-order accuracy. To achieve this, we primarily rely on a periodic Fourier extension u_e of u with a suitably large period b . We demonstrate the accuracy and efficiency of the proposed integration scheme through a variety of numerical

n	WFS		FS	
	ε_n	noc	ε_n	noc
2^5	9.8×10^{-1}	—	1.0×10^{-0}	—
2^6	4.5×10^{-1}	1.1	6.2×10^{-2}	4.0
2^7	1.8×10^{-1}	1.4	2.9×10^{-3}	4.4
2^8	1.4×10^{-1}	0.4	6.8×10^{-4}	2.0
2^9	7.3×10^{-2}	0.9	1.6×10^{-4}	2.1
2^{10}	2.1×10^{-2}	1.8	4.7×10^{-5}	1.8

TABLE 14. A convergence study for a plane wave scattering by penetrable square cavity Ω in Example 10, where the contrast function $m(x) = -1$ in Ω and zero outside.

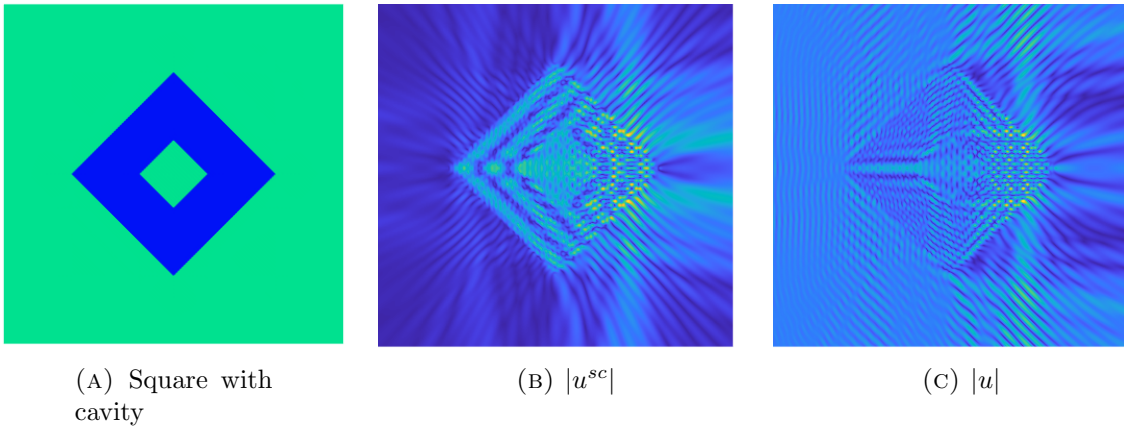


FIGURE 9. Scattering of a plane wave by penetrable square cavity Ω of acoustic size $\kappa a = 128$ when contrast function $m(x) = -1$ in Ω and zero outside. A computational grid of size 512×512 is used for this simulation.

experiments. We see that the rate of convergence of the method increases with increasing smoothness of the periodic extension. In fact, the method exhibits super-algebraic convergence when the extension is infinitely differentiable. Furthermore, when the density has jump discontinuities, we employ a certain Fourier smoothing technique to accelerate the convergence to achieve the quadratic rate. We utilize the integration scheme for numerical solution of certain partial differential equations and to obtain a fast and high-order Nystöm solver for the solution of the Lippmann-Schwinger integral equation.

We observe that the rate of convergence of the proposed scheme depends on g and the smoothness of u_e . The numerical experiments indicate that the computational error behaves as

$$\|Au - A_n u\|_\infty \leq O\left(n^{-(2+r+\min(0,\beta-1))}\right),$$

provided u_e is r times continuously differentiable in \mathbb{R}^2 with Lipschitz continuous $u_e^{(r+1)}$, that is, $u_e \in C^{r,1}(\mathbb{R}^2)$ and g is such that $|\widehat{g}(k)| \leq C_g(1 + |k|^2)^{-\beta/2}$ for some constant C_g . The error analysis to rigorously establish this behaviour is an interesting future research effort. The implementation and analysis of the method to three and higher dimensions is another future research direction of significant interest.

ACKNOWLEDGMENTS

AA acknowledges the support by Science & Engineering Research Board through File No. MTR/2017/000643. AKT & AP acknowledge the Initiation Grant from the Indian Institute of Science Education and Research Bhopal.

REFERENCES

- [1] J. Aguilar and Y. Chen, *A high-order, fast algorithm for scattering calculation in two dimensions*, Computers and Mathematics with Applications, (47) (2004), pp. 1–11.
- [2] F. Andersson and A. Holst, *A fast, bandlimited solver for scattering problems in inhomogeneous media*, Journal of Fourier Analysis and Applications, 11 (2005), pp. 471–487.
- [3] W. Bao, S. Jiang, Q. Tang, and Y. Zhang, *Computing the ground state and dynamics of the nonlinear Schrödinger equation with nonlocal interactions via the nonuniform FFT*, Journal of Computational Physics, 296 (2015), pp. 72–89.
- [4] W. Bao, Q. Tang, and Y. Zhang, *Accurate and efficient numerical methods for computing ground states and dynamics of dipolar Bose-Einstein condensates via the nonuniform FFT*, Communications in Computational Physics, 19 (2016), pp. 1141–1166.
- [5] G. Beylkin, C. Kurcz, and L. Monzón, *Fast convolution with the free space Helmholtz Green’s function*, Journal of Computational Physics, 228 (2009), pp. 2770–2791.
- [6] O. P. Bruno and E. M. Hyde, *An efficient, preconditioned, high-order solver for scattering by two-dimensional inhomogeneous media*, Journal of Computational Physics, 200 (2004), pp. 670–694.
- [7] O. P. Bruno and E. M. Hyde, *Higher-order Fourier approximation in scattering by two-dimensional, inhomogeneous media*, SIAM Journal on Numerical Analysis, 42 (2005), pp. 2298–2319.
- [8] O. P. Bruno and A. Pandey, *Fast, higher-order direct/iterative hybrid solver for scattering by inhomogeneous media—with application to high-frequency and discontinuous refractivity problems*, arXiv preprint arXiv:1907.05914, (2019).
- [9] M. Charnley and A. Wood, *Object identification in radar imaging via the reciprocity gap method*, Radio Science, 55 (2020), p. e2019RS006946. e2019RS006946 10.1029/2019RS006946.
- [10] R. Coifman, V. Rokhlin, and S. Wandzura, *The fast multipole method for the wave equation: a pedestrian prescription*, IEEE Antennas and Propagation Magazine, 35 (1993), pp. 7–12.
- [11] D. Colton and P. Monk, *A linear sampling method for the detection of leukemia using microwaves*, SIAM Journal on Applied Mathematics, 58 (1998), pp. 926–941.
- [12] D. Colton and P. Monk, *A linear sampling method for the detection of leukemia using microwaves II*, SIAM Journal on Applied Mathematics, 60 (1999), pp. 241–255.
- [13] D. L. Colton, R. Kress, and R. Kress, *Inverse acoustic and electromagnetic scattering theory*, vol. 93, Springer, 1998.
- [14] E. Darve, *The fast multipole method: Numerical implementation*, Journal of Computational Physics, 160 (2000), pp. 195–240.
- [15] R. Duan and V. Rokhlin, *High-order quadratures for the solution of scattering problems in two dimensions*, Journal of Computational Physics, 228 (2009), pp. 2152–2174.
- [16] H. Elman, D. J. Silvester, and A. J. Wathen, *Finite Elements and Fast Iterative Solvers : with Applications in Incompressible Fluid Dynamics*, Oxford University Press, 2005.
- [17] F. Ethridge and L. Greengard, *A new fast-multipole accelerated Poisson solver in two dimensions*, SIAM Journal on Scientific Computing, 23 (2001), pp. 741–760.

- [18] L. Exl, N. J. Mauser, and Y. Zhang, *Accurate and efficient computation of nonlocal potentials based on Gaussian-sum approximation*, Journal of Computational Physics, 327 (2016), pp. 629–642.
- [19] L. Genovese, T. Deutsch, A. Neelov, S. Goedecker, and G. Beylkin, *Efficient solution of Poisson’s equation with free boundary conditions*, The Journal of Chemical Physics, 125 (2006), p. 074105.
- [20] I. S. Gradshteyn and I. M. Ryzhik, *Table of integrals, series, and products*, Elsevier/Academic Press, Amsterdam, seventh ed., 2007.
- [21] L. Greengard and V. Rokhlin, *A new version of the fast multipole method for the Laplace equation in three dimensions*, Acta Numerica, 6 (1997), pp. 229–269.
- [22] A. J. Hesford and R. C. Waag, *The fast multipole method and Fourier convolution for the solution of acoustic scattering on regular volumetric grids*, Journal of computational physics, 229 (2010), pp. 8199–8210.
- [23] E. M. Hyde and O. P. Bruno, *A fast, higher-order solver for scattering by penetrable bodies in three dimensions*, Journal of Computational Physics, 202 (2005), pp. 236–261.
- [24] L.-M. Imbert-Gerard, F. Vico, L. Greengard, and M. Ferrando, *Integral equation methods for electrostatics, acoustics, and electromagnetics in smoothly varying, anisotropic media*, SIAM Journal on Numerical Analysis, 57 (2019), pp. 1020–1035.
- [25] O. Marin, O. Runborg, and A.-K. Tornberg, *Corrected trapezoidal rules for a class of singular functions*, IMA Journal of Numerical Analysis, 34 (2014), pp. 1509–1540.
- [26] P. A. Martin, *Acoustic scattering by inhomogeneous obstacles*, SIAM Journal on Applied Mathematics, 64 (2003), pp. 297–308.
- [27] A. Pandey and A. Anand, *Fourier smoothed pre-corrected trapezoidal rule for solution of Lippmann-Schwinger integral equation*, arXiv preprint arXiv:2007.06293, (2020).
- [28] T.-a. Pham, E. Soubies, A. Ayoub, J. Lim, D. Psaltis, and M. Unser, *Three-dimensional optical diffraction tomography with Lippmann-Schwinger model*, IEEE Transactions on Computational Imaging, 6 (2020), pp. 727–738.
- [29] F. Vico, L. Greengard, and M. Ferrando, *Fast convolution with free-space Green’s functions*, Journal of Computational Physics, 323 (2016), pp. 191–203.

AWANISH KUMAR TIWARI, DEPARTMENT OF MATHEMATICS, INDIAN INSTITUTE OF SCIENCE EDUCATION AND RESEARCH BHOPAL, MP 462066
Email address: awanisht@iiserb.ac.in

AMBUJ PANDEY, DEPARTMENT OF MATHEMATICS, INDIAN INSTITUTE OF SCIENCE EDUCATION AND RESEARCH BHOPAL, MP 462066
Email address: ambuj@iiserb.ac.in

COMPUTATIONAL & MATHEMATICAL SCIENCES, CALIFORNIA INSTITUTE OF TECHNOLOGY
Email address: jpaul@caltech.edu

AKASH ANAND, DEPARTMENT OF MATHEMATICS AND STATISTICS, INDIAN INSTITUTE OF TECHNOLOGY, KANPUR, UP 208016
Email address: akasha@iitk.ac.in